



Article

Tuning the Metal–Insulator Transition Properties of VO₂ Thin Films with the Synergetic Combination of Oxygen Vacancies, Strain Engineering, and Tungsten Doping

Mohamed A. Basyooni ^{1,2,3}, Mawaheb Al-Dossari ^{4,5}, Shrouk E. Zaki ^{1,3}, Yasin Ramazan Eker ^{3,6,*}, Mucahit Yilmaz ² and Mohamed Shaban ^{7,8,*}

- ¹ Department of Nanotechnology and Advanced Materials, Graduate School of Applied and Natural Science, Selçuk University, Konya 42030, Turkey; m.a.basyooni@gmail.com (M.A.B.); shrouk.e.zaki@gmail.com (S.E.Z.)
 - ² Department of Nanoscience and Nanoengineering, Institute of Science and Technology, University of Necmettin Erbakan, Konya 42060, Turkey; mucahityilmaz@erbakan.edu.tr
 - ³ Science and Technology Research and Application Center (BITAM), University of Necmettin Erbakan, Konya 42060, Turkey
 - ⁴ Research Center for Advanced Materials Science (RCAMS), King Khalid University, Abha 61413, Saudi Arabia; mdosri@kku.edu.sa
 - ⁵ Department of Physics, Dhahran Aljanoub, King Khalid University, Abha 61421, Saudi Arabia
 - ⁶ Department of Metallurgy and Material Engineering, Faculty of Engineering and Architecture, Necmettin Erbakan University, Konya 42060, Turkey
 - ⁷ Department of Physics, Faculty of Science, Islamic University of Madinah, AlMadinah Almonawara 42351, Saudi Arabia
 - ⁸ Nanophotonics and Applications Laboratory, Physics Department, Faculty of Science, Beni-Suef University, Beni-Suef 62514, Egypt
- * Correspondence: yecker@erbakan.edu.tr (Y.R.E.); mssfadel@aucegypt.edu (M.S.)



Citation: Basyooni, M.A.;

Al-Dossari, M.; Zaki, S.E.; Eker, Y.R.; Yilmaz, M.; Shaban, M. Tuning the Metal–Insulator Transition Properties of VO₂ Thin Films with the Synergetic Combination of Oxygen Vacancies, Strain Engineering, and Tungsten Doping. *Nanomaterials* **2022**, *12*, 1470. <https://doi.org/10.3390/nano12091470>

Academic Editors: Alain Pignolet and Christian Mitterer

Received: 8 March 2022

Accepted: 20 April 2022

Published: 26 April 2022

Publisher's Note: MDPI stays neutral with regard to jurisdictional claims in published maps and institutional affiliations.



Copyright: © 2022 by the authors. Licensee MDPI, Basel, Switzerland. This article is an open access article distributed under the terms and conditions of the Creative Commons Attribution (CC BY) license (<https://creativecommons.org/licenses/by/4.0/>).

Abstract: Vanadium oxide (VO₂) is considered a Peierls–Mott insulator with a metal–insulator transition (MIT) at $T_c = 68^\circ\text{C}$. The tuning of MIT parameters is a crucial point to use VO₂ within thermoelectric, electrochromic, or thermochromic applications. In this study, the effect of oxygen deficiencies, strain engineering, and metal tungsten doping are combined to tune the MIT with a low phase transition of 20°C in the air without capsulation. Narrow hysteresis phase transition devices based on multilayer VO₂, WO₃, Mo_{0.2}W_{0.8}O₃, and/or MoO₃ oxide thin films deposited through a high vacuum sputtering are investigated. The deposited films are structurally, chemically, electrically, and optically characterized. Different conductivity behaviour was observed, with the highest value towards VO_{1.75}/WO_{2.94} and the lowest VO_{1.75} on FTO glass. VO_{1.75}/WO_{2.94} showed a narrow hysteresis curve with a single-phase transition. Thanks to the role of oxygen vacancies, the MIT temperature decreased to 35°C , while the lowest value ($T_c = 20^\circ\text{C}$) was reached with Mo_{0.2}W_{0.8}O₃/VO₂/MoO₃ structure. In this former sample, Mo_{0.2}W_{0.8}O₃ was used for the first time as an anti-reflective and anti-oxidative layer. The results showed that the MoO₃ bottom layer is more suitable than WO₃ to enhance the electrical properties of VO₂ thin films. This work is applied to fast phase transition devices.

Keywords: thin films; vanadium oxide; thermochromic; phase transition device; metal–insulator transition

1. Introduction

VO₂ is one of the simplest correlated oxide materials, with a metal–insulator transition (MIT) phase transition at 68°C [1]. The semiconductor phase was observed at low temperatures with a monoclinic crystal structure. In contrast, at high temperatures, it is a tetragonal rutile structure [2]. VO₂ is the most intensively investigated solid-state thermochromic, metamaterials, and switching terahertz device [3–5]. It is still not ready for industrial or commercial application due to several problems. For instance, the transition temperature at 68°C is too high for applications in daily life (such as intelligent window applications).

This issue can be overcome since the conductivity of VO₂ can be changed with different doping elements, which can control the phase transition (T_c) value. For example, W⁶⁺ and Mo⁶⁺ increase the electron concentrations by tending to the metallic state, decreasing the T_c [6,7]. Despite the considerable difference in the elementary particle amount between elements ¹⁸⁴W & ⁹⁶Mo, they can contribute similarly to the VO₂ structure. Based on the Hume-Rothery rules, VO₂, MoO₃, and WO₃ can crystallize in the same or compatible structure. Simultaneously, +6 oxidation state, the ionic radii of these nuclei are close to Mo⁶⁺: 62 pm, W⁶⁺: 60 pm, and V⁴⁺: 58 pm. On the other hand, elements with lower valence, such as Cr³⁺ or Al³⁺, have also been used as doping elements [8]. The luminous transmittance of VO₂ at 50% (or less) is too low for daily use, which should be increased for real applications. Moreover, the solar energy modulation between the VO₂'s two states is modest, which should be considered. Research efforts are targeted at overcoming the above issues. For instance, T_c can be modulated to a suitable temperature via doping, which depends on many factors such as the charge and size of the dopant ion and the change of electron carrier density. A multilayer structure is adopted to improve the luminous transmittance of VO₂ coating. However, enhancing these factors together requires to combine effects such as oxygen vacancies and strain engineering, as reported below.

Oxygen vacancies on transition metal oxide surfaces (or in bulk) can alter the host system's electronic structure and chemical properties, even influencing VO₂ electric properties. As a result, the properties of the vacancies would be primarily determined by the host system. The defect reaction defines the formation of an oxygen vacancy $O_O^X \rightarrow \frac{1}{2}O_2(g) + V_O^\bullet + 2e'$. When the host crystal contains a cation with several stable oxidation states, the reaction will be of the type $O_O^X + M_M^X \rightarrow \frac{1}{2}O_2(g) + V_O^\bullet + 2M_M'$. To maintain charge neutrality, an oxygen vacancy can be formed by delocalized or localized compensation by donating electrons to the conduction band or reducing cations in the host material, respectively [9]. There are still difficulties in the experimental determination of the vacancy-induced lattice relaxations and information about the vacancy formation energy (hence defect stability) in VO₂ and V₂O₅ [10]. The electron doping induced by oxygen vacancies suppressed the MIT's lower temperature in oxygen-deficient VO₂ [11]. It can decrease the transition temperature to room temperature or even lower [12]. Zhang et al. reported a low-temperature oxidation annealing process (LTP) to prolong the oxygenation time of the oxygen-deficient VO₂, to understand the role of oxygen vacancy in the structure and MIT of VO₂ [13]. Since VO_{2-x} is more strain-sensitive than pure VO₂, combining the effects of oxygen vacancy and compressive strain could effectively tune phase transition behaviour and lower phase transition temperatures [14]. For 2D Van der Waals (VDWs) structures, VO₂ plays a prominent role in compressive strain, resulting in a shift in Raman modes of MoS₂, especially in the photoluminescence of trion peak to lower energy [15].

Moreover, the role of grain boundaries on the MIT of VO₂ is also interesting. By combining plasmon resonance nano spectroscopy with density functional calculations, Appavoo et al. studied the role of defects in the MIT on lithographically defined VO₂ nanoparticles. They showed that the most likely point defect nucleating the phase transition in MIT is an oxygen vacancy present at grain boundaries created by strain [16].

In this work, the preparation and characterization of multilayer WO₃, Mo_{0.2}W_{0.8}O₃, and MoO₃ in contact with monoclinic VO₂ (M-VO₂) is reported. Optical, electrical, structural, morphological, and topographical characterizations are performed. This study is concerned with tuning the electrical properties and the temperature phase transition of monoclinic VO₂ thin film on glass substrates for phase-change devices and applications. The effect of oxygen vacancy, strain engineering, and metal tungsten doping were simultaneously combined to tune the Metal-Insulator Transition (MIT) for the first time based on multilayer thin films. Many combinations based on VO₂, WO₃, Mo_{1-x}W_xO₃, and/or MoO₃ thin films are covered here to combine the effects of oxygen vacancy, strain effects, and doping effects. Due to the high optical transmission of Mo_{1-x}W_xO₃, these layers are inserted at the top of the structure to work as an anti-reflection layer and anti-oxidation, as reported in our recent study [17]. To obtain information about the oxidation state of

the prepared monoclinic VO₂ layer, several characterizations such as X-ray photoelectron spectroscopy (XPS) are reported.

2. Materials and Methods

2.1. Preparation of Thin Films

The samples were produced in a VAKSIS-MİDAS-3M1T magnetron sputter system (VAKSIS, Ankara, Turkey). Figure 1 shows the schematic diagram of the multilayer structure of the device. There are two 13.56 MHz power supplies and one DC power supply in the system with three magnetrons. Multilayer thin films were fabricated from 3 inch and 99.9% purity vanadium, molybdenum, and tungsten metallic targets by reactive sputtering. Argon and oxygen gases connected to the magnetron sputter system had a purity of 99.98%. Before starting the sputtering process, the FTO substrates were cleaned with acetone and isopropyl alcohol by keeping them in an ultrasonic cleaner for 15 min. They were then rinsed with deionized water and dried with high-purity nitrogen gas. After the substrates placed in the magnetron sputter holder were placed into the system, the system started to vacuum and was reduced to a 9.3×10^{-7} mbar pressure level. After reaching the desired pressure level, the sample holder was heated to 400 °C. It was kept at this temperature for 30 min for the temperature to stabilize on the substrate. Abbreviations of sample names and all deposition parameters are summarized in Table 1. The system pressure was increased to 6.8×10^{-3} mbar for the reactive sputter process for all samples. Time-dependent thickness optimization was achieved by using samples that had been produced in different thicknesses and whose thickness measurements had been made before. This optimization was used in sample fabrications as shown in Table 1. By controlling the film deposition times, the thicknesses of V–O, W–O, Mo–O, and Mo–W–O films were kept constant for all samples. The Mo_{0.2}W_{0.8}O₃ thin film is a composite film of Mo and W, in the presence of a 12.1 sccm oxygen environment. Whereas, the Ar flow is 50 sccm. The Mo and W powers are 27 and 110 W, respectively. The deposition time was 16.7 min during the whole process for both Mo and W targets. The idea here is to introduce a small amount of Mo atoms into the WO₃ film to form a high-quality anti-refractive anti-oxidative layer. In addition, this layer provides high transmission and good electrical performance, as predicted from our previous work [15,17]. The optimization of the content of Mo into WO₃ has been covered before [17,18].

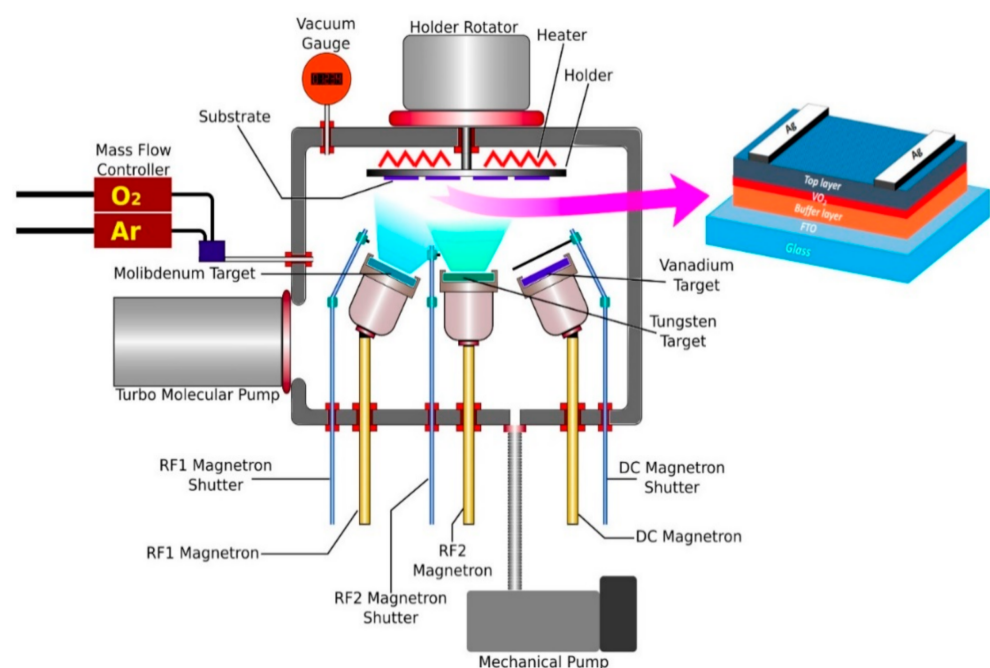


Figure 1. A schematic diagram for the used RF and DC sputtering system.

Table 1. Abbreviation of samples and deposition parameters of the multilayer films.

Notation	Structure	Layer	Power of Mo (W) RF1	Power of W (W) RF2	Power of V (W) DC	Ar Flow (sccm)	O ₂ Flow (sccm)	Time (min)
S1	VO ₂	1st layer: VO ₂	-	-	190	41	2.2	7.5
S2	VO ₂ /MoO ₃	1st layer: MoO ₃	137	-	-	37.1	12.1	16.7
		2nd layer: VO ₂	-	-	190	41	2.2	7.5
S3	VO ₂ /WO ₃	1st layer: WO ₃	-	137	-	37.1	12.1	7.5
		2nd layer: VO ₂	-	-	190	41	2.2	7.5
S4	WO ₃ /VO ₂ /MoO ₃	1st layer: MoO ₃	137	-	-	37.1	12.1	16.7
		2nd layer: VO ₂	-	-	190	41	2.2	7.5
		3rd layer: WO ₃	-	137	-	37.1	12.1	7.5
S5	Mo _{0.2} W _{0.8} O ₃ /VO ₂ /MoO ₃	1st layer: MoO ₃	137	-	-	37.1	12.1	16.7
		2nd layer: VO ₂	-	-	190	41	2.2	7.5
S6	Mo _{0.2} W _{0.8} O ₃ /VO ₂ + W/MoO ₃	3rd layer: Mo _{0.2} W _{0.8} O ₃	27	110	-	37.1	12.1	7.5
		1st layer: MoO ₃	137	-	-	37.1	12.1	16.7
		2nd layer: VO ₂ + W	-	10	190	41	2.2	7.5
		3rd layer: Mo _{0.2} W _{0.8} O ₃	27	110	-	37.1	12.1	7.5

2.2. Characterization Techniques

The optical transmission (T) result was measured using UV-VIS-NIR Spectrophotometer (UV-3600i Plus, Shimadzu, Tokyo, Japan). The topography of the films was studied using Atomic Force Microscopy Park XE7 system (Park, Santa Clara, CA, USA) with a scanning area of $1 \times 1 \mu\text{m}^2$, and a tip scan speed of 0.5 Hz, through noncontact mode. The crystal structures were analysed using X-ray diffraction GNR ADP PRO 2000 (GNR Srl, Novara, Italy) with a radiation source of $\text{CuK}\alpha$ ($\lambda = 1.5405 \text{ \AA}$) step of 0.01. These data were refined via the Rietveld method applied using Fullprof suite software (Version 5 January 2021) to determine the exact metal-oxygen concentrations of each layer and different phases. The surface morphology was recorded using field-emission scanning electron microscopy (FESEM, GeminiSEM 500, ZEISS, Cambridge, UK). The energy dispersive X-ray (EDX) analysis of the samples was carried out to characterize the quantitative analyses of the samples using an Oxford, Xmax 50 SEM (Oxford Instruments, Oxford, UK) attached with an Oxford EDS detector. Raman vibrational modes were obtained using Renishaw inVia confocal Raman microscope (Renishaw, New Mills, UK) using 532 nm laser beam with 10 mW laser power. X-ray photoelectron spectroscopy (XPS) measurements were carried out on the Thermo Scientific K-alpha XPS system (Thermo Scientific™, Waltham, MA, USA) using an $\text{AlK}\alpha$ source and a spot size of 400 μm . Fourier Transform Infrared Spectrometer (FTIR) through a 200–4000 nm range were collected with Thermo Scientific-Nicolet iS20 (Waltham, MA, USA). The electrical I–V phase transition measurements were taken using a 2450 Keithley Source Meter (Tektronix, Beaverton, OR, USA) and a four-probe system in which a heating stage is connected. The thicknesses of the samples were measured using the thin film analyzer system F20-UV (FILMETRICS, San Diego, MA, USA) with a ± 1 nm error. The values are as follows: S1 (VO₂) is 50.651 nm, S2 (VO₂/MoO₃) is 150.726 nm, S3 (VO₂/WO₃) is 148.908 nm, S4 (WO₃/VO₂/MoO₃) is 248.983 nm, S5 (Mo_{0.2}W_{0.8}O₃/VO₂/MoO₃) is 269.302 nm, and S6 (Mo_{0.2}W_{0.8}O₃/VO₂ + W/MoO₃) is 276.672 nm.

3. Results and Discussion

3.1. Characterization of FTO Supported Oxide Thin Film

The samples studied in this work are based on the successive deposition of metal oxide thin film. Therefore, the preparation conditions regarding each desired layer on FTO glass have been optimized. Typically used, the Raman spectra show the successful preparation of each thin film (Figure 2). Within the VO₂ layer (also used as sample S1), the peaks related to lattice motion involving V–V bonds (132 and 229 cm⁻¹) as well as the vibrational mode of V–O bonds in the VO₂ monoclinic insulating phase (500 & 828 cm⁻¹) are the most critical [19–23]. For the MoO₃ thin film, the most robust peaks at 820, 860, and 994 cm⁻¹ are related to the α-MoO₃ crystal phase and the M–O stretching modes [24–26]. The weaker peaks at 190, 283, 336, and 352 cm⁻¹ are based on Mo–O’s bending mode [27,28], while the one at 658 cm⁻¹ is assigned to triply coordinated oxygen Mo₃–O stretching [29]. Concerning the WO₃ layer, the monoclinic phase is characterized by peaks at 270 and 326 cm⁻¹ [30]. The structure is confirmed via the WO₃ lattice mode peak at 132 cm⁻¹ [31] and the stretching mode peaks of W–O–W bonding at 711 & 810 cm⁻¹ [30]. Finally, the Raman peaks for Mo_{0.2}W_{0.8}O₃ thin films are very weak. However, the prominent peaks for the WO₃ are distinguishable, suggesting a severe disruption of the WO₃ structure with the introduction of Mo. Nevertheless, Raman spectroscopy is not accurate enough for the precision of the structural properties of thin films, which strongly influence their thermochromic performance.

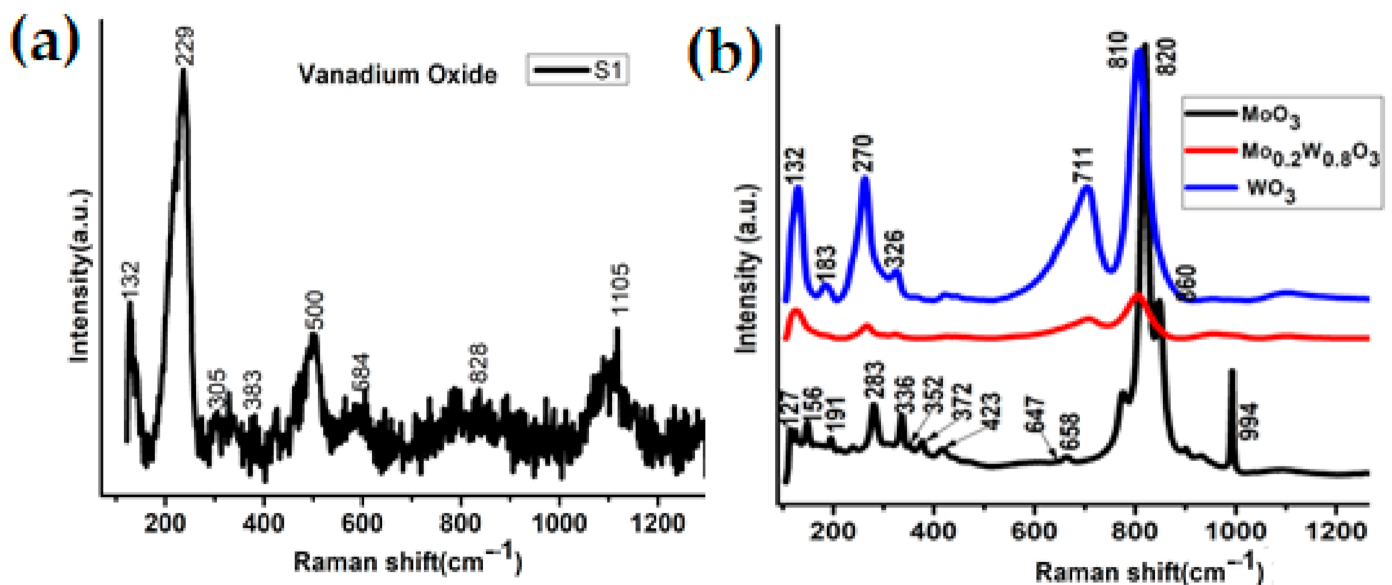


Figure 2. Raman spectra of the one-layer-based phase transition devices. (a) Characteristic Raman peaks of vanadium oxide (S1). (b) Characteristic Raman peaks of tungsten trioxide, molybdenum trioxide, and molybdenotungsten trioxide thin films.

Mo, W, and V metals are metal atoms with large coordination numbers, and the number of phases with oxygen is also large. Some of these phases are metastable, while others are stable. Synthesis conditions such as temperature, oxygen ratio, and deposition pressure are the basic parameters that determine the phase to be formed. The X-ray diffractogram has been used to determine the oxidation state and the structural parameters of the thin films (V–O, W–O, Mo–O, and Mo–W–O) as in Figure 3a, separately. These XRD patterns were obtained by GIXRD examination of thick films (>300 nm) grown on Soda-Lime Glass (SLG) under the same conditions for each layer. The examination was carried out with a grazing angle of 1° and counting for 5 s at each angle value in 0.01° steps. XRD patterns presented separately for each layer were used to determine the phase or phases of the thin film structure. Rietveld structure refinement was performed with the technique

described in [17] for Mo–O, and Mo–W–O, W–O phases and the technique described in [32] for the VO₂ phase, using the FullProf Suite software, which yielded the structure parameters and stoichiometric ratios of metal and oxygen. The use of Rietveld refinement to characterize the structural properties and concentration of vacancies is a frequently used method, reported in numerous reported studies [17,32–37]. However, performing structural analysis with XRD patterns that occur when XRD is taken for multilayer structures brings some errors. In the resulting multilayer structure, XRD peaks will occur in a very complex order and it will be difficult to determine which phase they belong to.

Vanadium oxide film shows a monoclinic phase with a space group of C₁₂/m1. The diffraction peaks observed at $2\theta = 27.9, 37.2, 42.3, 55.6,$ and 57.7° refer to (011), (200), (212), (220), and (022), respectively. The main peak is observed for $2\theta = 27.9^\circ$, indicating a preferential orientation toward the (011) plan. The diffractogram corresponds roughly to the VO₂ structure. However, the oxygen defects detected via the refinement show the presence of the VO_{1.75} compound. The oxygen vacancies act as electron donors with high n-type conductivity. They can alter the electron orbital occupancy and the band structure of the V–O layer [32,38]. VO_{1.75} layer is a rutile metallic state [39–41] which is unstable due to its sensitivity to atmospheric oxygen. Tungsten oxide film shows a monoclinic phase (γ -WO_{2.94}) with a space group of P₁₂/m1. This phase is also maintained for the Mo–W–O layer (Mo_{0.2}W_{0.8}O_{2.8}). Concerning the molybdenum oxide (MoO₃), the diffractogram corresponds to an orthorhombic structure with the Pnma space group. However, this layer is biphasic, consisting of 40% MoO_{2.08} and 60% MoO_{3.01}. Thus, an oxygen deficiency for each layer has been observed, confirming their metallic characteristic. On the other hand, the XRD patterns of each layer present the central peak at around 23° , which corresponds to the plan (002) of the monoclinic phase and (011) of the orthorhombic structure. The atomic alignment with an angle of 90° for both plans allows overlaying. This characteristic is also true for the plan (011) of the V–O layer. That is why the heterojunction is probably obtained following these orientations within the multilayer structure.

However, the widths of the XRD peaks give us a rough value of the crystallite size with the help of the Debye–Scherrer equation. The crystallite size was calculated from the Debye–Scherrer equation ($D = 0.9\lambda/\beta\cos\theta$). After that, the main peak positions (2θ) and their corresponding FWHM (β), crystalline size (D), dislocation density (δ , where $\delta = 1/D^2$), and microstrain (ϵ , where $\epsilon = \beta/4\tan\theta$) were estimated (Table 2). Although this value is not exact, it is valuable in terms of speculating. Decreased peak widths indicate an increase in crystallite size. It is important to note that the XRD of WO₃ shows crystalline and amorphous phases together. As the growth temperature of the W–O film is 400°C , this temperature is close to the W–O crystallization temperature. The W–O structure crystallizes in the range of $400\text{--}600^\circ\text{C}$ [42].

In order to calculate the FWHM for the crystallite size in the structures containing W–O, a deconvolution was performed using the PeakFit software (Version 4.12), assuming a Lorentzian-shaped peak located at about 23 degrees. The crystallite size calculated for Mo–O was found to be larger than the W–O film. It was also found to be relatively small for the Mo–W–O layer. Penetration of Mo into the W–O layer resulted in a reduction of the main peak width. With the incorporation of Mo atoms into the W–O structure, an expected increase in the crystallite size, hence in the crystallinity, occurred, and it can be said that W–O crystal structures is maintained even in the presence of Mo atoms. Thus, the crystallinity of the oxide layers is improved with the presence of Mo in contrarily to W [43]. The calculation shows that the crystallite size for the W–O film (5.5 nm) is much smaller than for Mo–O (17.0 nm), while the crystallite size for Mo–W–O is intermediate (6.0 nm). However, the largest crystallites were calculated for the V–O layer with 20.5 nm. The evolution of the crystallite size values is inversely proportional to the evolution of dislocation density and microstrain. In other words, small crystallite size, high dislocation density, and high microstrain were calculated for W–O thin film. In contrast, the opposite was calculated for Mo–O and V–O layers. Nevertheless, all values are low for Mo–W–O thin film, suggesting that the Mo doping can add new properties to the W–O-based thin film.

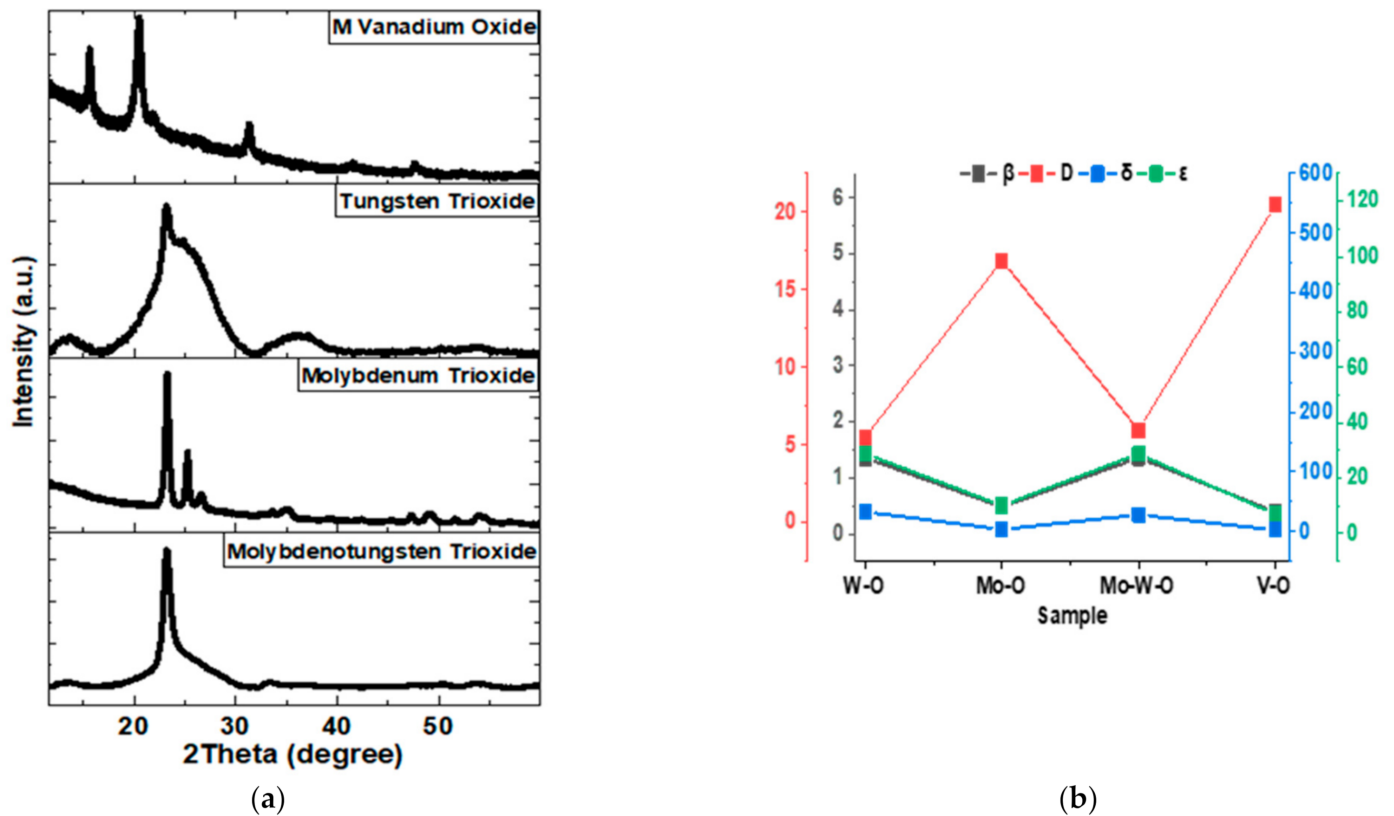


Figure 3. (a) XRD spectra of vanadium oxide, tungsten trioxide, molybdenum trioxide, and molybdenotungsten trioxide films. Where (b) summarizes the relationship between the FWHM (β in (°)), the crystallite size (D in (nm)), dislocation density (δ in (nm⁻²)), microstrain (ϵ in (unitless)) of each layer.

Table 2. Shows the main peak position, corresponding FWHM, crystallite size, dislocation density, and microstrain of the samples.

Sample	2θ (°)	β (°)	D (nm)	$\delta \times 10^{-3}$ (nm ⁻²)	$\epsilon \times 10^{-3}$
V-O	27.936	0.399	20.5	2.4	7.01
Mo-O	23.254	0.479	17.0	3.5	10.18
Mo-W-O	23.309	1.359	6.0	28.1	28.76
W-O	23.222	1.358	5.5	32.9	28.84

3.2. Effect of the Buffer Layer on the VO₂ Properties

The MIT properties of the multi-layer oxide structure are governed via the behaviour of the VO₂ layer. As seen above, the buffer layer (WO₃ and MoO₃) effect on vanadium-based oxide has been studied (S1–S3). Raman spectroscopy analysis of these structures S2–S6 is depicted in Figure S1 (supplementary information). Similar peaks are observed for these structures, as have been reported above for the single layers. The topographical analysis of MoO₃ and WO₃ deposited only on the glass substrate is investigated as in Figure S2.

First of all, the morphology of the VO₂ thin film is strongly influenced by the buffer layer (Figure 4). The VO₂ layer, as deposited on the FTO glass (S1), consists of small particles (about 20 nm as predicted with XRD) homogeneously and densely distributed. Table 3 provided information about the topographic data of S1–S6 samples. The mean grain area is below $9.5 \times 10^{-3} \mu\text{m}^2$, involving a very low average roughness (Ra). However, when deposited on the MoO₃ layer (S2), VO₂ grains are bigger, and aggregates are visible on the surface. The average roughness is more than 12 times bigger than for S1, according

to the relief observed on the FESEM picture. Concerning the WO₃ bottom layer (S3), small particles completely disappear, and clusters with nano leaves are present on the surface of the VO₂ thin film. Even if the mean grain area reaches more than $1.77 \times 10^{-3} \mu\text{m}^2$, Ra values are only about 6 nm. This effect has been ascribed to the monoclinic crystal structure of WO₃ film, which favours electron diffusion [44]. Finally, these three samples confirm that the VO₂ thin film morphology is sensitive to any internal or external strain or stimuli [45,46].

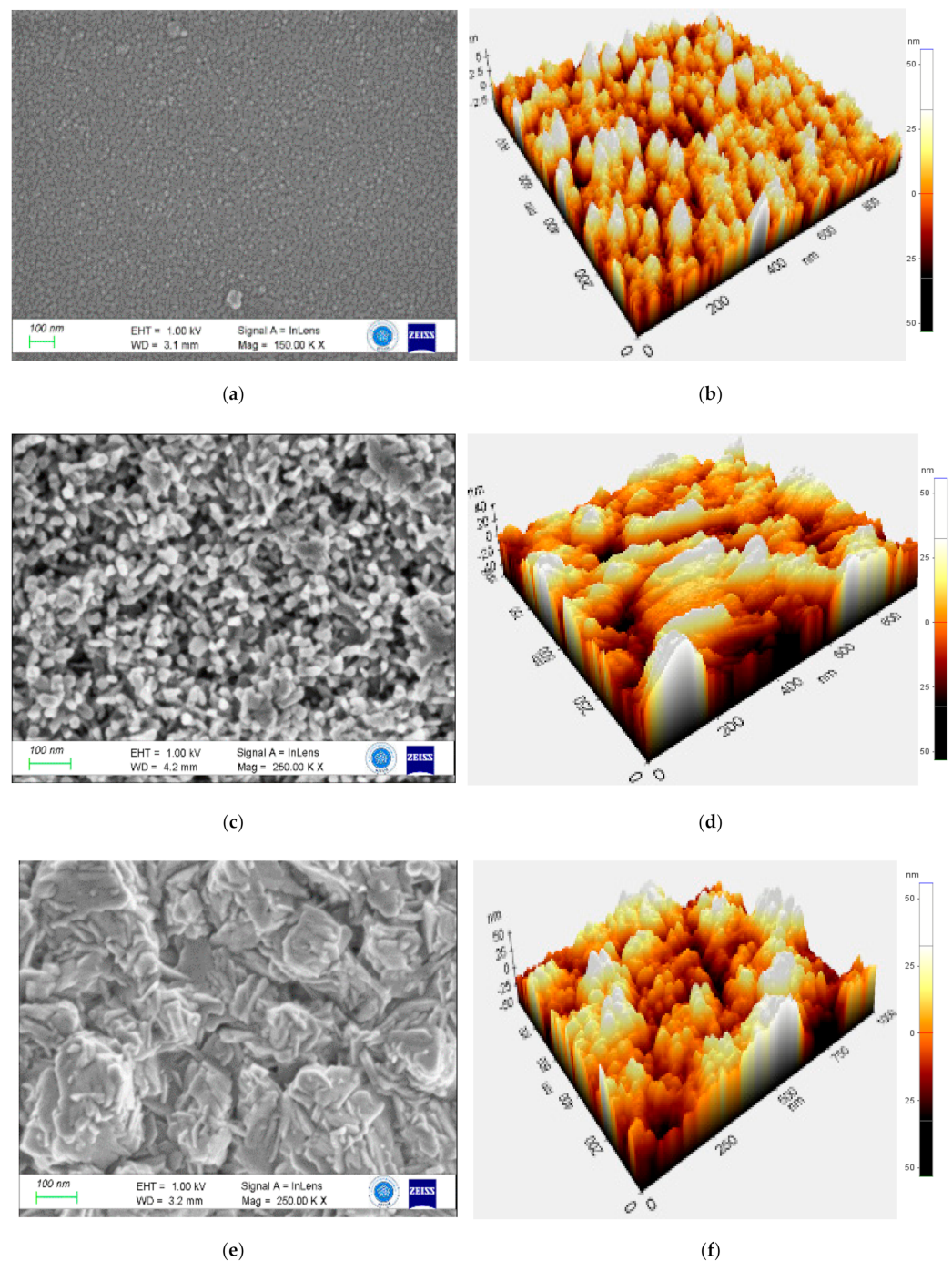


Figure 4. Morphological and topographical analysis of S1 (a,b), S2 (c,d), and S3 (e,f) samples, respectively.

Used as support for metal oxide layers, it is known that FTO glass is transparent at more than 70% on the UV-visible-NIR domains. However, the optical properties are different according to the metal oxide layers (Figure S3). The transparency is reducing below 40% for the VO₂ layer. However, for the Mo–O, Mo–W–O, and W–O layers, the transparency can reach values higher than 80% up to almost 100% Mo–W–O at around 500 nm.

On the other hand, the surface bonding is also affected by the effect of the buffer layer. The vanadium binding on the XPS spectrum of the film supported with WO₃ (S3) is characteristic of highly oxidized vanadium (V⁴⁺/V⁵⁺) at around 517 and 524 eV [47–49]. While peaks are related to low oxidation (V³⁺) at around 41 and 68 eV when supported with MoO₃ (S2) (Figure 5a,b) [50,51]. In other words, the interaction between molybdenum and vanadium oxides allows for keeping an oxidation degree below 4. In contrast, the vanadium-based layer is more sensitive to oxidation when supported with WO₃. Therefore, MoO₃ has been preferred as a buffer layer for the samples aiming to study the anti-reflective top layer effect on the thermochromic properties of vanadium oxide. In addition, the observed signals of Na, Ca, Sn, and Si stem from the thin layer of the FTO glass substrate. It is important to mention that all films were deposited with high vacuum sputtering techniques, with ultrahigh homogenous depositions. These conditions avoid the absence of covering some parts during the deposition of S2. The diffusion of some elements from the substrate into the S2 is highly expected during the film deposition. This is because the films were deposited at an approximately high temperature of 400 °C, followed by an in situ annealing at 400 °C for around 2 h. These two processes may cause direct diffusion of some elements from the substrate into the film.

Table 3. Topographic data of S1–S6 samples.

Sample	Mean Grain Area (μm ²)	R _a (nm)	R _q (nm)	R _{pv} (nm)
S1	9.41 × 10 ^{−4}	0.9	1.2	6.8
S2	1.183 × 10 ^{−3}	12.2	14.1	56.1
S3	1.774 × 10 ^{−3}	6.0	7.4	33.5
S4	1.056 × 10 ^{−3}	10.1	12.1	49.9
S5	1.526 × 10 ^{−3}	5.7	6.9	28.1
S6	9.06 × 10 ^{−4}	13.8	16.1	63.1

R_a: Average roughness, R_q: root mean square or standard deviation of the height value, and R_{pv}: height difference or peak-to-valley.

3.3. Anti-Reflective Top Layer Surface State

Due to their optical properties of WO₃ (S4) and Mo_{0.2}W_{0.8}O₃ (S5) were coated in situ on the surface of MoO₃ supported VO₂ layer. Both surfaces contain particles that locally aggregate, inducing pores formation between them (Figure 6). The topographic data show that the surface roughness of S4 is comparable to S2. The WO₃ top layer can fit the structure of the VO₂ thin film. However, when 20% W is substituted with Mo within the top layer (S5), its particle's grain area increases from 1.183 × 10^{−3} to 1.526 × 10^{−3} μm², involving lower surface roughness. The former presents smaller particles and higher roughness when deposited on W doping of the VO₂ (S6). The multilayer morphological and topographical analysis demonstrates that the surface is dependent mainly on the bottom layer state and, to a lesser extent, on the upper layer properties.

3.4. FTIR Spectroscopic, Optical Properties, and Urbach Tail

Here, we investigated the optical properties of the deposited thin film with UV-visible-NIR spectroscopy and FTIR spectroscopy, as depicted in Figure S4 (supplementary information). The FTIR spectrum of S1 presents three prominent absorption peaks at around 400, 766, and 901 cm^{−1} (Figure S4a). Even if they are attributed to the V–O stretching mode for the lowest wavenumber [52] and lattice vibration mode for the two others [53,54],

these peaks are not Gaussian. However, the UV-visible-NIR spectroscopy shows the optical transmission as in Figure S4b. Introducing W into the VO₂ structure improves the transparency close to the support values. This evolution can probably be explained by two reasons, the electron density evolution of the local crystal strain introduction within the VO₂ layer.

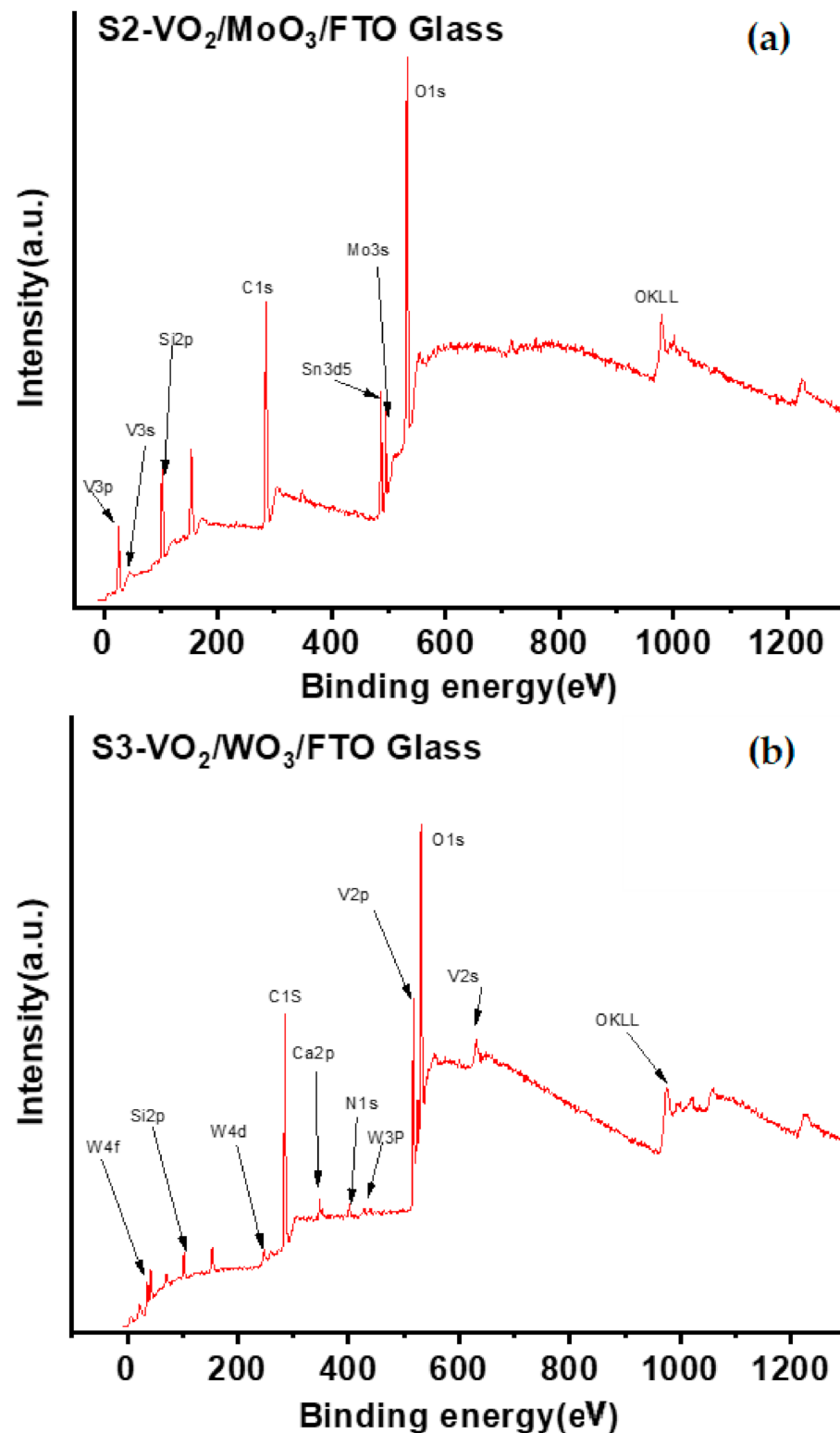


Figure 5. Fast XPS scan of some selected samples: (a) S2 and (b) S3.

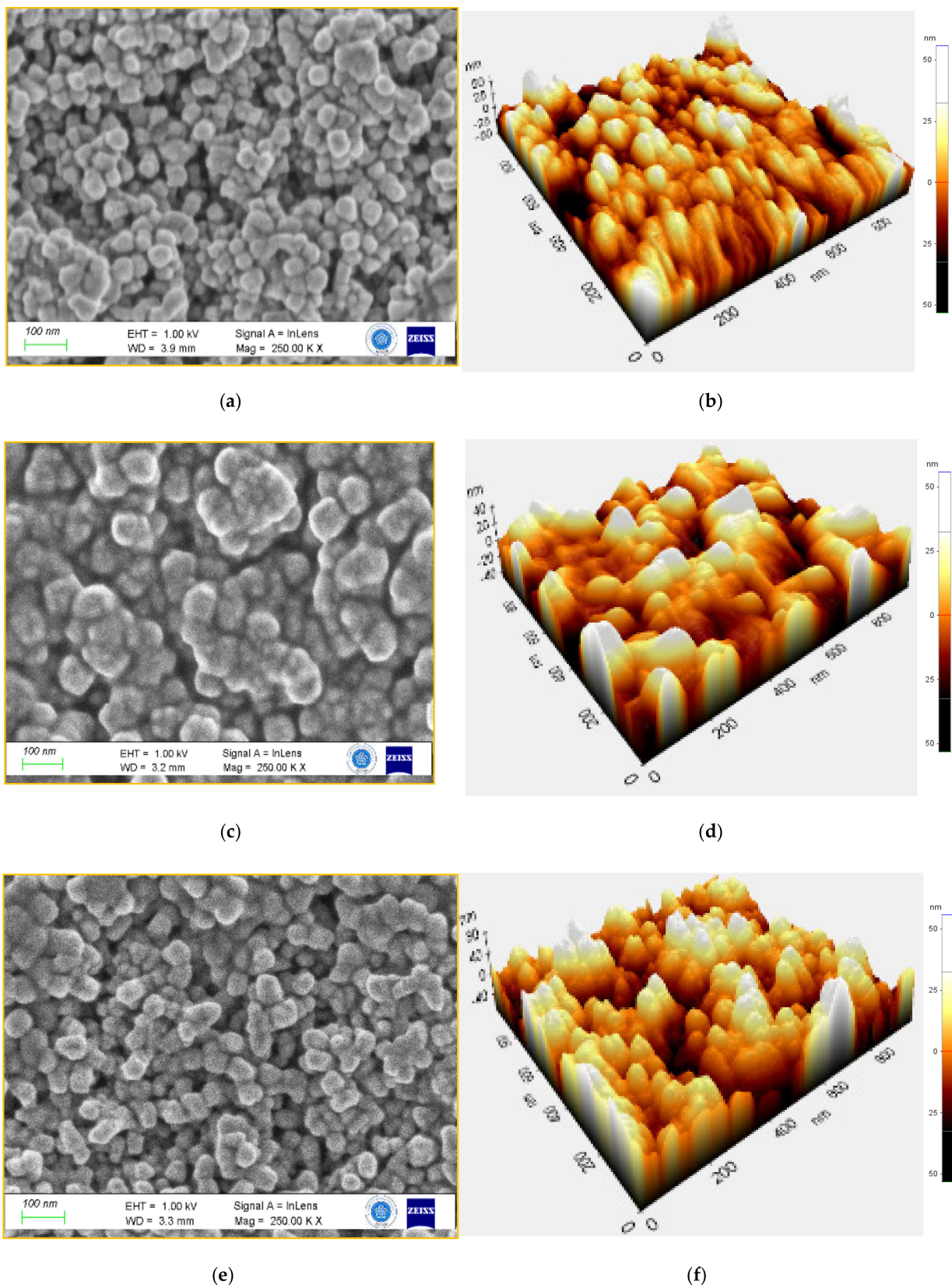


Figure 6. Morphological and Topographical analysis of S4 (a,b), S5 (c,d), and S6 (e,f) samples.

The calculation of the Urbach energy (E_U) evolution provides a clue concerning the transmittance fall observed (Figure S5a,b). E_U is visible in low crystalline, disordered, or amorphous materials with localized states in the standard bandgap due to exciton/phonon

or electron/phonon interactions. The results show that with the modification of the VO₂ structure, the electronic transitions from band to tail and tail to tail are facilitated with probably a better order between the layers [55]. Thus, the combination Mo_{0.2}W_{0.8}O₃/W-VO₂/MoO₃ is optimum regarding the optical properties of the present materials.

3.5. Electric Properties

Due to the specificity of the correlated oxide, the evolution of the structural, optical, and electrical properties is parallel with temperature. Thus, following the electrical properties is an alternative to understanding the MIT characteristics. An Ohmic behaviour is observed at room temperature for S1 and S2. In contrast, a Schottky contact is detected for the others (S3 to S6) (Figure 7a). However, the most resistive sample is S1, and the most conductive are S3 and S4, which are the only ones containing the WO₃ layer. More than the samples' multilayer and grain structure, the influence of the intrinsic conductivity of WO₃ is the most important parameter [56]. As seen above, WO₃ favours the formation of V₂O₅, which is the highest oxidative state among the vanadium oxides and the most resistive [57]. On the other hand, the presence of WO₃ and/or MoO₃ layers does not significantly affect samples' response time, contrarily to the samples (S5 and S6) where the Mo_{0.2}W_{0.8}O₃ layer is involved (Figure 7b). Whatever the combination, after roughly 9 s, the resistance of multilayer samples reaches the low values. Since Mo_{0.2}W_{0.8}O₃ contains similarly WO₃, MoO₂, and MoO₃ phases, and electrons diffusion are probably deleted within this layer. Finally, except for S1 which is purely resistive, the other samples present a semi-conductive behaviour.

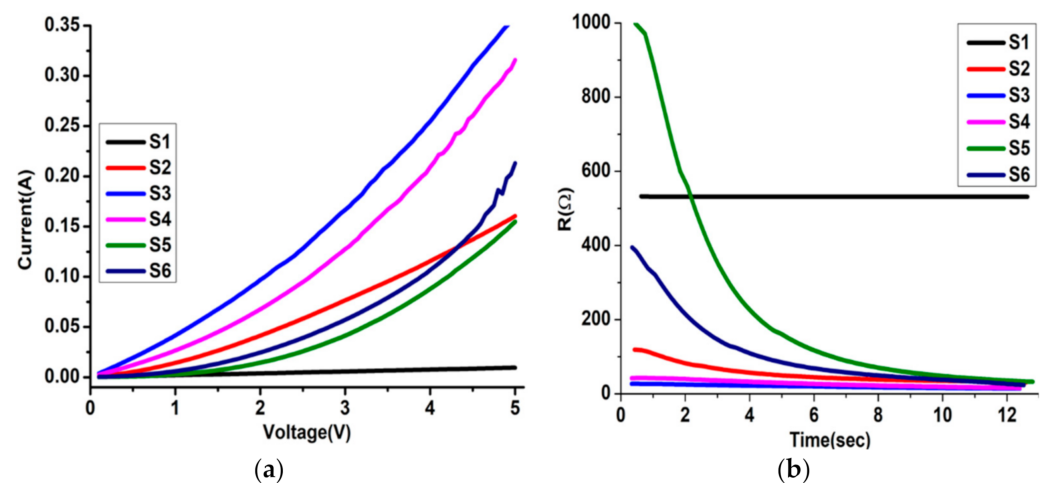


Figure 7. (a) The characteristic I–V curves of S1–S6 thin films and (b) the corresponding change in R–t curves of the measured I–V curves of each film.

The VO₂ phase change from monoclinic to tetragonal crystal structure with temperature involves the decrease of the resistivity. Therefore, the MIT value (also denoted T_c) for each structure can be evaluated by following the electrical properties of the samples. When a sharp decrease is not observed in the resistivity, the measured MIT will be considered from the starting point of the decrease. In this work, the MIT for all samples is lower than the theoretical value T_c = 68 °C for VO₂ (Figure 8a,f). According to the characterization above, the typical profile for the VO₂ (VO_{1.73}) layer is observed for S1. The low MIT at about 35 °C is due to the oxygen vacancies [58,59].

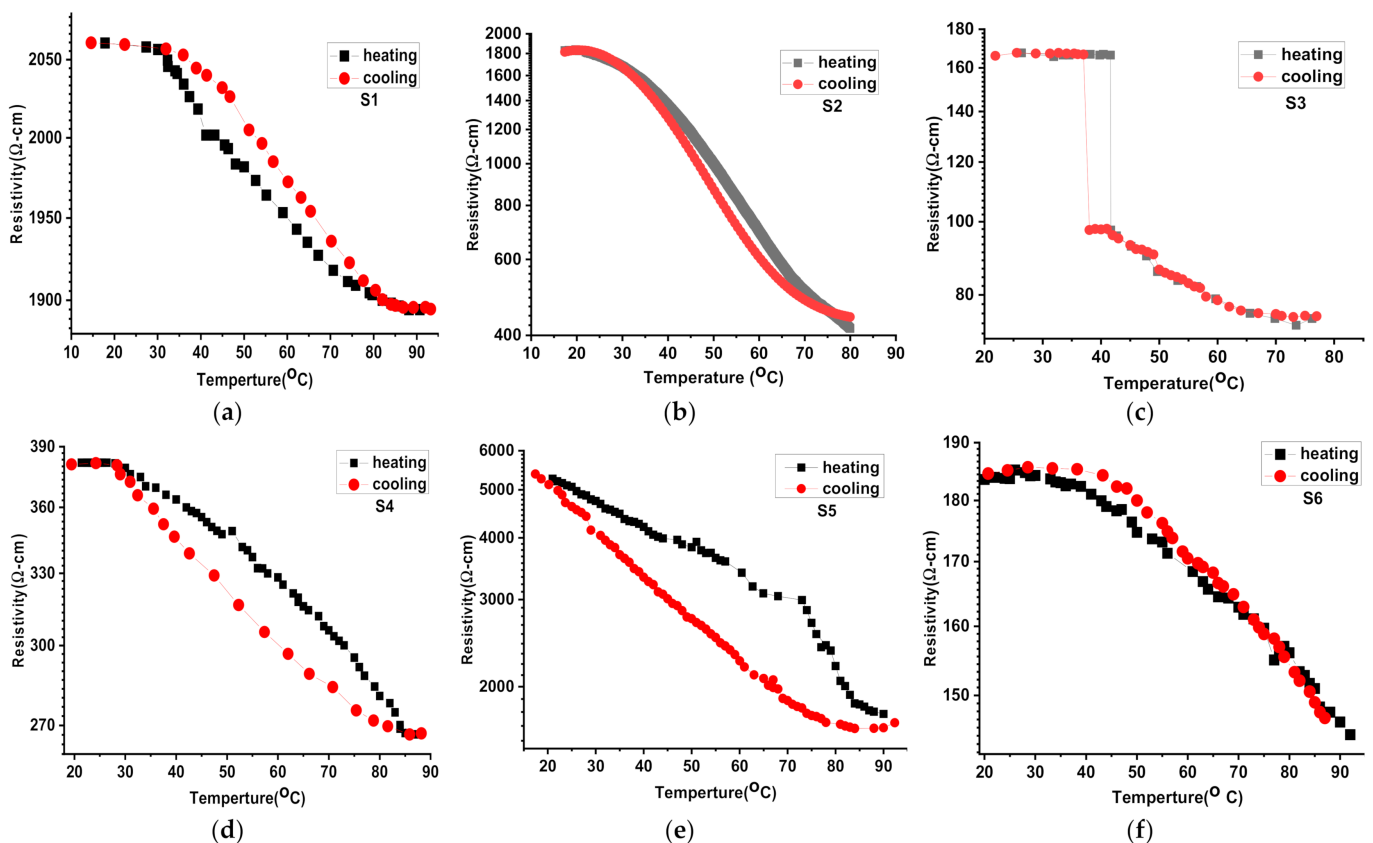


Figure 8. Electric properties and phase transition characterization measurements of the prepared S1–S6 (a–f) thin films.

Nevertheless, the high resistivity values and the hysteresis observed between the heating and cooling curves show a forced transition phase. When deposited on MoO_3 (S2), the VO_2 phase transition starts at lower T_c (25 °C), and the hysteresis dramatically disappears. The strain effect of MoO_3 combined with the oxygen deficiency is profitable; however, the resistivity is still high. The resistivity is significantly reduced when WO_3 is a bottom layer (S3), and a sharp resistivity decrease appears at 41 °C during heating. The T_c is higher than for S1, but the theoretical abrupt decrease is only visible with this sample.

On the other hand, the lowest resistivity value is not reached at 41 °C, and the XPS results from the formation of V_2O_5 at the film surface. Therefore, it is suggested that WO_3 contributes to improving the structure's conductivity. However, probably due to its insufficient strain effect, it cannot prevent the oxidation of VO_2 to V_2O_5 , the most stable vanadium oxide. Currently, WO_3 is used as an anti-reflective layer. Therefore, sandwich structure with MoO_3 at the bottom and WO_3 at the upper layer was investigated with S4. As expected, the MIT was reduced to $T_c = 30$ °C, and the resistivity values were low. Unfortunately, a critical hysteresis appears. Since the presence of Mo seems to facilitate the strain effect and based on the performance demonstrated within our previous work, $\text{Mo}_{0.2}\text{W}_{0.8}\text{O}_3$, which is a Mo doped WO_3 thin film, was tested as the upper layer (S5). The lower MIT temperature (about 20 °C) and the highest resistivity values are reached, and a critical hysteresis is observed with S5. The introduction of Mo within the WO_3 structure involves the simultaneous presence of MoO_2 , MoO_3 , and WO_3 . The presence of MoO_3 possibly contributes to the strain of the VO_2 structure. However, it also disrupts the WO_3 continuity involving a drop in the conductivity. Due to its confirmed anti-reflective and anti-oxidative performance, $\text{Mo}_{0.2}\text{W}_{0.8}\text{O}_3$ was kept as the upper layer. W-doped VO_2 was designed to decrease the sample S6 resistivity. The W doping is exceedingly profitable in decreasing the hysteresis and the resistivity of the structure. However, T_c increases to up to 36 °C. Therefore, thanks to the sandwich structure prepared with two doped thin films, the

hysteresis and the resistivity decreased significantly by almost keeping the reference T_c . Based on the literature reviews, we conclude that our study is a facile and efficient way to modulate the phase transition of VO₂ thin film as in Table 4.

Table 4. Summary of the previous studies and the advantages of our current study.

Structure	Preparation Method	Tunneling Effect	Phase Transition Temperature	Ref.
Cr-doped VO ₂	Pulsed laser deposition	Doping	34 °C	[57]
Mo-doped VO ₂	DC sputtering	Doping	63 °C	[58]
W-doped VO ₂	Sol-gel	Doping	36 °C	[47]
W-doped VO ₂	DC sputtering	Doping	37.4 °C	[59]
Al-doped VO ₂	DC sputtering	Doping	44.9 °C	[60]
V ₂ O ₅ /metal V/V ₂ O ₅ , V ₂ O ₅ /metal W/V ₂ O ₅ multilayers	RF sputtering	Sandwich structure	55 °C 48 °C	[61]
VO ₂ on MgF ₂ (110)	Oxide MBE method	Interfacial strain and oxygen vacancies	69 °C	[62]
W-doped VO ₂	Hydrothermal	Doping	31.64 °C	[63]
VO ₂	Sol-gel dip coating	-	68 °C	[64]
Mo _{0.2} W _{0.8} O ₃ / VO ₂ /MoO ₃	DC, RF Sputtering	Oxygen vacancy concentration, lattice strain, and W-doping effects	20 °C	This work

4. Conclusions

VO₂ is one of the most investigated phase transition materials since the MIT is observed close to ambient temperature. According to the application, setting the T_c is a crucial parameter. In this study, the MIT temperature decreased to 41 °C via oxygen-vacancy vanadium dioxide (VO_{1.73}) through the deposition conditions. The evolution of the bandgap and the Urbach tail demonstrate the influence of the bottom and top layers on the VO₂ layer. These interactions are probably guided by the common vibration observed in the Raman spectrum between two layers which have an interface. The results showed that the structure of the VO₂ layer is more preserved when MoO₃ is used than WO₃. The electrical measurements show that the structure resistance is lower, and the phase transition is easier with the WO₃ bottom layer. On the other hand, WO₃ does not reduce the hysteresis between the heating and cooling curve contrarily to MoO₃. The former decreases the T_c down to 25 °C, and the hysteresis is significantly reduced. Therefore, the combination of MoO₃ bottom layer and WO₃ upper layer was investigated with the WO₃/VO₂/MoO₃, in which resistance is low, T_c of VO₂ is kept, but the hysteresis is still present. Meanwhile, the high microstrain on VO_{1.75} film of 119.9×10^{-3} is exerted by the monoclinic WO_{2.94} buffer layer, which contributed to a fast and sharp phase transition WO_{2.94}/VO_{1.75}/FTO glass with a low phase transition. The transmittance of Mo-doped WO₃ (Mo_{0.2}W_{0.8}O₃) is higher than WO₃, and the dislocation density is comparable to the VO₂ layer. The potential of Mo_{0.2}W_{0.8}O₃ as an alternative upper layer was confirmed with Mo_{0.2}W_{0.8}O₃/VO₂/MoO₃, where the T_c decreases to 20 °C. Nonetheless, the hysteresis and the resistance are incredibly increasing. To maintain the profit of Mo_{0.2}W_{0.8}O₃ and improve the conductivity of the sample, VO₂ was doped with metallic W. The combination Mo_{0.2}W_{0.8}O₃/VO₂-W/MoO₃ successfully showed low T_c at 36 °C, low resistivity at tens of ohm, and no hysteresis. Thanks to this study, the synergy between oxygen deficiency, strain engineering, and metal doping was reached for improving the MIT characteristics of VO₂ thin film.

Supplementary Materials: The following supporting information can be downloaded at: <https://www.mdpi.com/article/10.3390/nano12091470/s1>, Figure S1: Raman spectra of the multi-layers-based phase transition devices. Figure S2: Topographical analysis of MoO₃ (a) and WO₃ (b). Figure S3: Transmission spectra (T) of the single-layer thin films. Figure S4: (a) FTIR spectra of samples S1–S6 at room temperature. (b) UV-Vis-NIR spectra of samples S1–S6 at room temperature. (c,d) the refractive index and extinction coefficient of S1–S6 thin films with wavelengths. Figure S5: (a) and (b) represent the plot of (Ln α) versus photon energy and the Urbach energy (Urbach tail) with bandgap for S1–S6 thin films, respectively. References [65–69] are cited in the supplementary materials.

Author Contributions: Conceptualization, M.A.B. and S.E.Z. methodology, M.A.B. and S.E.Z.; validation, M.A.B., S.E.Z., Y.R.E., M.Y., M.A.-D. and M.S.; formal analysis, M.A.B., S.E.Z., Y.R.E. and M.Y.; investigation, M.A.B., S.E.Z., M.Y. and Y.R.E.; resources, M.A.B., S.E.Z., M.Y., Y.R.E., M.A.-D. and M.S.; data curation, M.A.B., S.E.Z. and M.S.; writing—original draft preparation, M.A.B., S.E.Z. and M.Y.; writing—review and editing, M.A.B., S.E.Z., Y.R.E., M.Y., M.A.-D. and M.S.; visualization, M.A.B., M.A.-D., M.S.; Supervision, Y.R.E. and M.Y.; project administration, M.A.B., M.A.-D. and M.S.; funding acquisition, M.A.B., M.A.-D. and M.S. All authors have read and agreed to the published version of the manuscript.

Funding: The APC was funded by the King Khalid University through a grant KKU/RCAMS/22 under the Research Center for Advance Materials (RCAMS) at King Khalid University, Saudi Arabia.

Data Availability Statement: The data presented in this study are available on request from the corresponding author.

Acknowledgments: This work was supported by the King Khalid University through a grant KKU/RCAMS/22 under the Research Center for Advance Materials (RCAMS) at King Khalid University, Saudi Arabia. The authors would like to express their gratitude to the Science and Technology Research and Application Centre of Necmettin Erbakan University (BITAM-NEU) for the ongoing assistance with the characterisation facilities.

Conflicts of Interest: The authors declare no conflict of interest.

References

1. Basu, R.; Sardar, M.; Dhara, S. Origin of phase transition in VO₂. In *AIP Conference Proceedings*; AIP Publishing LLC: Melville, NY, USA, 2018; Volume 1942, p. 030003.
2. Morin, F.J. Oxides which show a metal-to-insulator transition at the neel temperature. *Phys. Rev. Lett.* **1959**, *3*, 34–36. [[CrossRef](#)]
3. Zheng, Z.; Zheng, Y.; Luo, Y.; Yi, Z.; Zhang, J.; Liu, Z.; Yang, W.; Yu, Y.; Wu, X.; Wu, P. A switchable terahertz device combining ultra-wideband absorption and ultra-wideband complete reflection. *Phys. Chem. Chem. Phys.* **2022**, *24*, 2527–2533. [[CrossRef](#)] [[PubMed](#)]
4. Zheng, Z.; Zheng, Y.; Luo, Y.; Yi, Z.; Zhang, J.; Liu, L.; Song, Q.; Wu, P.; Yu, Y.; Zhang, J. Terahertz perfect absorber based on flexible active switching of ultra-broadband and ultra-narrowband. *Opt. Express* **2021**, *29*, 42787. [[CrossRef](#)]
5. Ren, Y.; Zhou, T.; Jiang, C.; Tang, B. Thermally switching between perfect absorber and asymmetric transmission in vanadium dioxide-assisted metamaterials. *Opt. Express* **2021**, *29*, 7666. [[CrossRef](#)]
6. Gao, Y.; Luo, H.; Zhang, Z.; Kang, L.; Chen, Z.; Du, J.; Kanehira, M.; Cao, C. Nanoceramic VO₂ thermochromic smart glass: A review on progress in solution processing. *Nano Energy* **2012**, *1*, 221–246. [[CrossRef](#)]
7. Hanlon, T.J.; Coath, J.A.; Richardson, M.A. Molybdenum-doped vanadium dioxide coatings on glass produced by the aqueous sol-gel method. *Thin Solid Films* **2003**, *436*, 269–272. [[CrossRef](#)]
8. Strelcov, E.; Tselev, A.; Ivanov, I.; Budai, J.D.; Zhang, J.; Tischler, J.Z.; Kravchenko, I.; Kalinin, S.V.; Kolmakov, A. Doping-based stabilization of the M2 phase in free-standing VO₂ nanostructures at room temperature. *Nano Lett.* **2012**, *12*, 6198–6205. [[CrossRef](#)]
9. Bergerudm, A.J. Phase Stability and Transformations in Vanadium Oxide Nanocrystals. Ph.D. Thesis, University of California, Berkeley, CA, USA.
10. Ganduglia-Pirovano, M.V.; Hofmann, A.; Sauer, J. Oxygen vacancies in transition metal and rare earth oxides: Current state of understanding and remaining challenges. *Surf. Sci. Rep.* **2007**, *62*, 219–270. [[CrossRef](#)]
11. Singh, S.; Abtew, T.A.; Horrocks, G.; Kilcoyne, C.; Marley, P.M.; Stabile, A.A.; Banerjee, S.; Zhang, P.; Sambandamurthy, G. Selective electrochemical reactivity of rutile VO₂ towards the suppression of metal-insulator transition. *Phys. Rev. B* **2016**, *93*, 125132. [[CrossRef](#)]
12. Liu, H.W.; Wong, L.M.; Wang, S.J.; Tang, S.H.; Zhang, X.H. Effect of oxygen stoichiometry on the insulator-metal phase transition in vanadium oxide thin films studied using optical pump-terahertz probe spectroscopy. *Appl. Phys. Lett.* **2013**, *103*, 151908. [[CrossRef](#)]

13. Zhang, J.; Zhao, Z.; Li, J.; Jin, H.; Rehman, F.; Chen, P.; Jiang, Y.; Chen, C.; Cao, M.; Zhao, Y. Evolution of Structural and Electrical Properties of Oxygen-Deficient VO₂ under Low Temperature Heating Process. *ACS Appl. Mater. Interfaces* **2017**, *9*, 27135–27141. [[CrossRef](#)] [[PubMed](#)]
14. Chen, L.; Cui, Y.; Shi, S.; Liu, B.; Luo, H.; Gao, Y. First-principles study of the effect of oxygen vacancy and strain on the phase transition temperature of VO₂. *RSC Adv.* **2016**, *6*, 86872–86879. [[CrossRef](#)]
15. Basyooni, M.A.; Zaki, S.E.; Shaban, M.; Eker, Y.R.; Yilmaz, M. Efficient MoWO₃/VO₂/MoS₂/Si UV Schottky photodetectors; MoS₂ optimization and monoclinic VO₂ surface modifications. *Sci. Rep.* **2020**, *10*, 15926. [[CrossRef](#)] [[PubMed](#)]
16. Appavoo, K.; Lei, D.Y.; Sonnefraud, Y.; Wang, B.; Pantelides, S.T.; Maier, S.A.; Haglund, R.F. Role of defects in the phase transition of VO₂ nanoparticles probed by plasmon resonance spectroscopy. *Nano Lett.* **2012**, *12*, 780–786. [[CrossRef](#)]
17. Basyooni, M.A.; Zaki, S.E.; Ertugrul, S.; Yilmaz, M.; Eker, Y.R. Fast response of CO₂ room temperature gas sensor based on Mixed-Valence Phases in Molybdenum and Tungsten Oxide nanostructured thin films. *Ceram. Int.* **2020**, *46*, 9839–9853. [[CrossRef](#)]
18. Currie, M.; Mastro, M.A.; Wheeler, V.D. Atomic layer deposition of vanadium dioxide and a temperature-dependent optical model. *J. Vis. Exp.* **2018**, *2018*, e57103. [[CrossRef](#)]
19. Li, Y.; Ji, S.; Gao, Y.; Luo, H.; Kanehira, M. Core-shell VO₂@TiO₂ nanorods that combine thermochromic and photocatalytic properties for application as energy-saving smart coatings. *Sci. Rep.* **2013**, *3*, 1370. [[CrossRef](#)]
20. Makarevich, A.M.; Sadykov, I.I.; Sharovarov, D.I.; Amelichev, V.A.; Adamenkov, A.A.; Tsybarenko, D.M.; Plokhii, A.V.; Esaulkov, M.N.; Solyankin, P.M.; Kaul, A.R. Chemical synthesis of high quality epitaxial vanadium dioxide films with sharp electrical and optical switch properties. *J. Mater. Chem. C* **2015**, *3*, 9197–9205. [[CrossRef](#)]
21. Chen, X.B. Assignment of the Raman modes of VO₂ in the monoclinic insulating phase. *J. Korean Phys. Soc.* **2011**, *58*, 100–104. [[CrossRef](#)]
22. Mohamed, B.; Ali, M. VO₂ İnce Film İçeren İki Boyutlu ve Çok Katmanlı Yapılardaki Arayüzey Gerilmelerinin Termokromik ve Fotodetektör Performanslara Etkisi. Master's Thesis, University of Necmettin Erbakan, Konya, Turkey, August 2020.
23. Nagyné-Kovács, T.; Studnicka, L.; Lukács, I.E.; László, K.; Pasierb, P.; Szilágyi, I.M.; Pokol, G. Hydrothermal synthesis and gas sensing of monoclinic MoO₃ nanosheets. *Nanomaterials* **2020**, *10*, 891. [[CrossRef](#)]
24. Martín-Ramos, P.; Fernández-Coppel, I.A.; Avella, M.; Martín-Gil, J. α -MoO₃ crystals with a multilayer stack structure obtained by annealing from a lamellar MoS₂/g-C₃N₄ nanohybrid. *Nanomaterials* **2018**, *8*, 559. [[CrossRef](#)] [[PubMed](#)]
25. Ivanova, T.; Gesheva, K.A.; Szekeres, A. Structure and optical properties of CVD molybdenum oxide films for electrochromic application. *J. Solid State Electrochem.* **2002**, *7*, 21–24. [[CrossRef](#)]
26. Kee, C.W. Assignment of O-O and Mo=O Stretching Frequencies of Molybdenum/Tungsten Complexes Revisited. *J. Chem.* **2015**, *2015*, 439270. [[CrossRef](#)]
27. Klinbumrung, A.; Thongtem, T.; Thongtem, S. Characterization of orthorhombic α -MoO₃ microplates produced by a microwave plasma process. *J. Nanomater.* **2012**, *2012*, 930763. [[CrossRef](#)]
28. Haque, F.; Zavabeti, A.; Zhang, B.Y.; Datta, R.S.; Yin, Y.; Yi, Z.; Wang, Y.; Mahmood, N.; Pillai, N.; Syed, N.; et al. Ordered intracrystalline pores in planar molybdenum oxide for enhanced alkaline hydrogen evolution. *J. Mater. Chem. A* **2019**, *7*, 257–268. [[CrossRef](#)]
29. Liu, F.; Chen, X.; Xia, Q.; Tian, L.; Chen, X. Ultrathin tungsten oxide nanowires: Oleylamine assisted nonhydrolytic growth, oxygen vacancies and good photocatalytic properties. *RSC Adv.* **2015**, *5*, 77423–77428. [[CrossRef](#)]
30. Díaz-Reyes, J.; Castillo-Ojeda, R.; Galván-Arellano, M.; Zaca-Moran, O. Characterization of WO₃ thin films grown on silicon by HFMOD. *Adv. Condens. Matter Phys.* **2013**, *2013*, 591787. [[CrossRef](#)]
31. Zaki, S.E.; Basyooni, M.A.; Shaban, M.; Rabia, M.; Eker, Y.R.; Attia, G.F.; Yilmaz, M.; Ahmed, A.M. Role of oxygen vacancies in vanadium oxide and oxygen functional groups in graphene oxide for room temperature CO₂ gas sensors. *Sens. Actuators A Phys.* **2019**, *294*, 17–24. [[CrossRef](#)]
32. Grey, I.E.; Wilson, N.C. Titanium vacancy defects in sol-gel prepared anatase. *J. Solid State Chem.* **2007**, *180*, 670–678. [[CrossRef](#)]
33. Jørgensen, J.E.; Mosegaard, L.; Thomsen, L.E.; Jensen, T.R.; Hanson, J.C. Formation of γ -Fe₂O₃ nanoparticles and vacancy ordering: An in situ X-ray powder diffraction study. *J. Solid State Chem.* **2007**, *180*, 180–185. [[CrossRef](#)]
34. Jiang, B.; Hou, N.; Huang, S.; Zhou, G.; Hou, J.; Cao, Z.; Zhu, H. Structural studies of TiC_{1-x}O_x solid solution by Rietveld refinement and first-principles calculations. *J. Solid State Chem.* **2013**, *204*, 1–8. [[CrossRef](#)]
35. Ferri, E.A.V.; Sczancoski, J.C.; Cavalcante, L.S.; Paris, E.C.; Espinosa, J.W.M.; de Figueiredo, A.T.; Pizani, P.S.; Mastelaro, V.R.; Varela, J.A.; Longo, E. Photoluminescence behavior in MgTiO₃ powders with vacancy/distorted clusters and octahedral tilting. *Mater. Chem. Phys.* **2009**, *117*, 192–198. [[CrossRef](#)]
36. Somogyvári, Z.; Sváb, E.; Mészáros, G.; Krezhov, K.; Nedkov, I.; Sajó, I.; Bourée, F. Vacancy ordering in nanosized maghemite from neutron and X-ray powder diffraction. *Appl. Phys. A Mater. Sci. Process.* **2002**, *74*, s1077–s1079. [[CrossRef](#)]
37. Fan, S.; Fan, L.; Li, Q.; Liu, J.; Ye, B. The identification of defect structures for oxygen pressure dependent VO₂ crystal films. *Appl. Surf. Sci.* **2014**, *321*, 464–468. [[CrossRef](#)]
38. Wang, X.; Wang, Z.; Zhang, G.; Jiang, J. Insight into Electronic and Structural Reorganizations for Defect-Induced VO₂ Metal-Insulator Transition. *J. Phys. Chem. Lett.* **2017**, *8*, 3129–3132. [[CrossRef](#)]
39. Liang, Y.C.; Chang, C.W. Preparation of orthorhombic WO₃ thin films and their crystal quality-dependent dye photodegradation ability. *Coatings* **2019**, *9*, 90. [[CrossRef](#)]
40. Liu, Y.; Patterson, B.R. Stereological analysis of Zener pinning. *Acta Mater.* **1996**, *44*, 4327–4335. [[CrossRef](#)]

41. Al Mohammad, A.; Gillet, M. Phase transformations in WO₃ thin films during annealing. *Thin Solid Films* **2002**, *408*, 302–309. [[CrossRef](#)]
42. Zhang, Y.; Xiong, W.; Chen, W.; Zheng, Y. Recent progress on vanadium dioxide nanostructures and devices: Fabrication, properties, applications and perspectives. *Nanomaterials* **2021**, *11*, 338. [[CrossRef](#)]
43. Ding, Z.; Cui, Y.; Wan, D.; Luo, H.; Gao, Y. High-performance thermal sensitive VO₂(B) thin films prepared by sputtering with TiO₂(A) buffer layer and first-principles calculations study. *RSC Adv.* **2017**, *7*, 29496–29504. [[CrossRef](#)]
44. Rosevear, W.H.; Paul, W. Hall effect in VO₂ near the semiconductor-to-metal transition. *Phys. Rev. B* **1973**, *7*, 2109–2111. [[CrossRef](#)]
45. Wang, S.; Malyshev, O.B.; Valizadeh, R.; Seddon, E.A.; Cropper, M.D. The secondary electron yield from transition metals. In Proceedings of the IPAC 2014 5th International Particle Accelerator Conference, Dresden, Germany, 16 June 2013–20 June 2014; pp. 2403–2405.
46. Zakharova, G.S.; Podval'Naya, N.V.; Kuznetsov, M.V. XPS study of nanorods of doped vanadium oxide M_x V₂O₅ · nH₂O (M = Na, K, Rb, Cs). *Russ. J. Inorg. Chem.* **2011**, *56*, 267–272. [[CrossRef](#)]
47. Pan, G.; Yin, J.; Ji, K.; Li, X.; Cheng, X.; Jin, H.; Liu, J. Synthesis and thermochromic property studies on W doped VO₂ films fabricated by sol-gel method. *Sci. Rep.* **2017**, *7*, 6132. [[CrossRef](#)] [[PubMed](#)]
48. Kong, F.Y.; Li, M.; Pan, S.S.; Zhang, Y.X.; Li, G.H. Synthesis and thermal stability of W-doped VO₂ nanocrystals. *Mater. Res. Bull.* **2011**, *46*, 2100–2104. [[CrossRef](#)]
49. Luo, Z.; Wu, Z.; Xu, X.; Wang, T.; Jiang, Y. Electrical and optical properties of nanostructured VO_x thin films prepared by direct current magnetron reactive sputtering and post-annealing in oxygen. *Thin Solid Films* **2011**, *519*, 6203–6207. [[CrossRef](#)]
50. Nam, S.P.; Noh, H.J.; Lee, S.G.; Lee, Y.H. Electrical properties of vanadium tungsten oxide thin films. *Mater. Res. Bull.* **2010**, *45*, 291–294. [[CrossRef](#)]
51. Vedeanu, N.; Cozar, O.; Stanescu, R.; Cozar, I.B.; Ardelean, I. Structural investigation of new vanadium-bismuth-phosphate glasses by IR and ESR spectroscopy. *J. Mol. Struct.* **2013**, *1044*, 323–327. [[CrossRef](#)]
52. Yoffe, A.D. Theory of Defects in Solids: Electronic Structure Defects in Insulators and Semiconductors. *Phys. Bull.* **1986**, *37*, 266–267. [[CrossRef](#)]
53. Tuo, S.; Cattin, L.; Essaidi, H.; Peres, L.; Louarn, G.; El Jouad, Z.; Hssein, M.; Touihri, S.; Yapi Abbe, S.; Torchio, P.; et al. Stabilisation of the electrical and optical properties of dielectric/Cu/dielectric structures through the use of efficient dielectric and Cu:Ni alloy. *J. Alloys Compd.* **2017**, *729*, 109–116. [[CrossRef](#)]
54. Kachi, S.; Takada, T.; Kosuge, K. Electrical Conductivity of Vanadium Oxides. *J. Phys. Soc. Jpn.* **1963**, *18*, 1839–1840. [[CrossRef](#)]
55. Gurunatha, K.L.; Sathasivam, S.; Li, J.; Portnoi, M.; Parkin, I.P.; Papakonstantinou, I. Combined Effect of Temperature Induced Strain and Oxygen Vacancy on Metal-Insulator Transition of VO₂ Colloidal Particles. *Adv. Funct. Mater.* **2020**, *30*, 2005311. [[CrossRef](#)]
56. Fan, L.; Wang, X.; Wang, F.; Zhang, Q.; Zhu, L.; Meng, Q.; Wang, B.; Zhang, Z.; Zou, C. Revealing the role of oxygen vacancies on the phase transition of VO₂ film from the optical-constant measurements. *RSC Adv.* **2018**, *8*, 19151–19156. [[CrossRef](#)]
57. Suleiman, A.O.; Mansouri, S.; Margot, J.; Chaker, M. Tuning VO₂ phase stability by a combined effect of Cr doping and oxygen pressure. *Appl. Surf. Sci.* **2022**, *571*, 151267. [[CrossRef](#)]
58. Batista, C.; Ribeiro, R.M.; Teixeira, V. Synthesis and characterization of VO₂-based thermochromic thin films for energy-efficient windows. *Nanoscale Res. Lett.* **2011**, *6*, 301. [[CrossRef](#)] [[PubMed](#)]
59. Huang, Z.; Wu, Z.; Ji, C.; Dai, J.; Xiang, Z.; Wang, D.; Dong, X.; Jiang, Y. Improvement of phase transition properties of magnetron sputtered W-doped VO₂ films by post-annealing approach. *J. Mater. Sci. Mater. Electron.* **2020**, *31*, 4150–4160. [[CrossRef](#)]
60. Ji, C.; Wu, Z.; Wu, X.; Wang, J.; Gou, J.; Huang, Z.; Zhou, H.; Yao, W.; Jiang, Y. Al-doped VO₂ films as smart window coatings: Reduced phase transition temperature and improved thermochromic performance. *Sol. Energy Mater. Sol. Cells* **2018**, *176*, 174–180. [[CrossRef](#)]
61. Liu, H.; Wan, D.; Ishaq, A.; Chen, L.; Guo, B.; Shi, S.; Luo, H.; Gao, Y. Sputtering Deposition of Sandwich-Structured V₂O₅/Metal (V, W)/V₂O₅ Multilayers for the Preparation of High-Performance Thermally Sensitive VO₂ Thin Films with Selectivity of VO₂ (B) and VO₂ (M) Polymorph. *ACS Appl. Mater. Interfaces* **2016**, *8*, 7884–7890. [[CrossRef](#)]
62. Fan, L.L.; Chen, S.; Liao, G.M.; Chen, Y.L.; Ren, H.; Zou, C.W. Comprehensive studies of interfacial strain and oxygen vacancy on metal-insulator transition of VO₂ film. *J. Phys. Condens. Matter* **2016**, *28*, 255002. [[CrossRef](#)]
63. Barra, H.M.; Chen, S.K.; Tamchek, N.; Talib, Z.A.; Lee, O.J.; Tan, K.B. Phase, Microstructure, Thermochromic, and Thermophysical Analyses of Hydrothermally Synthesized W-Doped VO₂ Nanopowder. *Adv. Mater. Sci. Eng.* **2021**, *2021*, 8582274. [[CrossRef](#)]
64. Chotirat, L.; Niyomwas, S.; Wongpisan, W.; Supothina, S. Low-Temperature Synthesis of Vanadium Dioxide Thin Films by Sol-Gel Dip Coating Method. *J. Nanotechnol.* **2021**, *2021*, 4868152. [[CrossRef](#)]
65. Görmez, A.E.; Basyooni, M.A.; Zaki, S.E.; Eker, Y.R.; Sönmez, E.; Yilmaz, M. Effect of in-/ex-situ annealing temperature on the optical, structural and gas sensing dynamics of CdS nanostructured thin films. *Superlattices Microstruct.* **2020**, *142*, 106536. [[CrossRef](#)]
66. Basyooni, M.A.M.A.; Shaban, M.; El Sayed, A.M.A.M. Enhanced Gas Sensing Properties of Spin-coated Na-doped ZnO Nanostructured Films. *Sci. Rep.* **2017**, *7*, 41716. [[CrossRef](#)] [[PubMed](#)]
67. Shportko, K.V. Disorder and compositional dependences in Urbach-Martienssen tails in amorphous (GeTe)_x(Sb₂Te₃)_{1-x} alloys. *Sci. Rep.* **2019**, *9*, 6030. [[CrossRef](#)] [[PubMed](#)]

-
68. Bonalde, I.; Medina, E.; Rodríguez, M.; Wasim, S.M.; Marín, G.; Rincón, C.; Rincón, A.; Torres, C. Urbach tail, disorder, and localized modes in ternary semiconductors. *Phys. Rev. B* **2004**, *69*, 195201. [[CrossRef](#)]
 69. Mishra, V.; Sagdeo, A.; Warshi, K.; Rai, H.M.; Saxena, S.; Kumar, R.; Sagdeo, P. Metastable behavior of Urbach tail states in BaTiO₃ across phase transition. *arXiv* **2016**, arXiv:1612.06756. Available online: <https://arxiv.org/abs/1612.06756v1> (accessed on 1 March 2022).